Inorganic Chemistry

pubs.acs.org/IC Article

Structural Disorder in Intermetallic Boride $Pr_{21}M_{16}Te_6B_{30}$ (M = Mn, Fe): A Transition Metal Cluster and Its Evil Twin

Tate O. Engstrand, Kaya Wei, Ryan Baumbach, Yan Xin, and Susan E. Latturner*

Cite This: *Inorg. Chem.* 2020, 59, 2484−2494 Read Online

ACCESS | Metrics & More | Article Recommendations | Supporting Information

ABSTRACT: Reactions of boron, tellurium, and either iron or manganese in a praseodymium−nickel flux led to the production of $Pr_{21}M_{16}Te_6B_{30}$ (M = Fe or Mn) with a novel structure type that features $M_{16}B_{30}$ clusters surrounded by a Pr/Te framework. Due to disorder in the orientation of the transition metal boride clusters, these phases initially appear to form in the cubic space group $Pm\bar{3}m$. However, analysis of site occupancy, bond lengths, and local structure in the $M_{16}B_{30}$ sublattice indicates the local symmetry is $P\bar{4}3m$. This space group symmetry is supported by transmission electron microscopy studies including selected area electron diffraction (SAED) and high angle annular dark field scanning transmission electron microscopy (HAADF-STEM), which indicate ordered regions. The $M_{16}B_{30}$ cluster twinning domain that could be as small as nanometer size inside a single crystal results in the misleading $Pm\bar{3}m$ symmetry. Electronic structure calculations indicate the $Pr_{21}M_{16}Te_6B_{30}$ phases are metals. Magnetic susceptibility measurements show that both the praseodymium and the transition metal have magnetic moments in these compounds. $Pr_{21}Mn_{16}Te_6B_{30}$ exhibits antiferromagnetic ordering at T_N = 15 K, and $Pr_{21}Fe_{16}Te_6B_{30}$ undergoes a likely ferrimagnetic transition at T_C = 23 K.

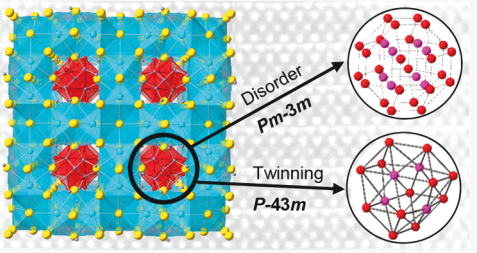

INTRODUCTION

Boron reacts readily with most metals, forming metal borides.[1] To date, more than 1000 binary and ternary metal borides with more than 150 different structure types are known.[1] These metal borides often feature covalent networks of boron in one, two, or three dimensions,[2] with the dimensionality of these arrangements scaling with the boron-to-metal ratio of the compounds.[3] The variety of bonding arrangements within each category has been shown to be due to the electron deficient nature of boron.[1−3] Boron atoms arrange into dumbbells in Ta_2OsB_2 and Nb_2RuB_2.[4,5] The intermetallic borides $Nb_6Fe_{1-x}Ir_{6+x}B_8$ and $Ti_7Rh_4Ir_2B_8$ contain isolated hexagonal rings.[6,7] Boride networks form double zigzag chains in Ta_3B_4.[8] WB_3 features graphene-like hexagonal boron sheets.[9] Three-dimensional networks are formed from B_4 ribbons in α-BeB_6 and from linked B_6 octahedra in LaB_6.[10,11] YB_{66} contains boron networks composed of interconnected B_{12} icosahedral clusters.[12]

The variety of metal boride structures and the strength of covalent boron−boron and metal−boron bonds give rise to a variety of interesting and useful characteristics.[1] The intermetallic borides $W_{0.93}Ta_{0.02}Cr_{0.05}B_4$ and $W_{0.92}Zr_{0.08}B_4$ are among the hardest materials known; both have a Vickers hardness exceeding 50 GPa at 0.49 N applied load.[13] While metal borides are well-known for their mechanical[13] and refractory[2] properties as well as their chemical stability,[14] many also display exotic behaviors like superconductivity (MgB_2 and $LaNi_2B_2C$).[15] The topological surface states of SmB_6 are protected by time-reversal symmetry.[16] SmB_{62} is a very-high temperature thermoelectric, with a ZT figure of merit approximately 40 times larger than that of other rare earth borides.[17] The resilience of boron-rich borides extends to nuclear chemistry, with single crystals of YB_{66} used as monochromators for soft synchrotron radiation in the 1−2 keV energy range.[18]

In addition to structural complexity, a number of transition metal borides feature complex magnetic behavior, which is dependent on the M−M bonding in the structure. The most famous industrial magnet, $Nd_2Fe_{14}B$, is an intermetallic boride featuring a 3-D network of iron encapsulating Nd^{3+} cations and interstitial boron atoms; it has an intrinsic coercivity of about 20 kOe and energy product of 14.1 MG Oe and is used in computer hard drives and electric motors.[19] The magneto-caloric material MnB is of interest since it is made from earth-abundant materials.[20] When the structural complexity includes disorder in the transition metal building blocks, the magnetic behavior can be affected significantly and potentially tailored. The magnetism of the borocarbide-capped $Fe_{14-x}Al_x$ clusters in $Ce_{33}Fe_{14-x}Al_xB_{25}C_{34}$ is quenched due to dilution by aluminum, in contrast to the ferromagnetic behavior of ordered clusters in the related phase $Ce_{33}Fe_{13}B_{18}C_{34}$.[21] Similarly, chains of Fe in $Ti_{9-n}Fe_{2+n}Ru_{18}B_8$ result in either ferro- or ferrimagnetism

Received: November 18, 2019
Published: February 3, 2020

https://dx.doi.org/10.1021/acs.inorgchem.9b03358
Inorg. Chem. 2020, 59, 2484−2494

depending on n.[22] Twinning disorder in magnetic alloys such as Ni_2MnGa result in the phenomenon of magnetically induced reorientation (MIR), in which the application of a magnetic field can cause the motion of twin domain walls and a resulting change in shape.[23,24] These compounds behave as magnetic shape memory alloys and are of interest as potential actuators and sensors.

In this work, we report on the synthesis and properties of new quaternary intermetallic borides with an unusual kind of twinning disorder, manifesting as variation in the orientation of transition metal clusters. The compounds $Pr_{21}M_{16}Te_6B_{30}$ (M = Mn, Fe) are grown from praseodymium−nickel fluxes. M_{16} clusters adopt a Friauf polyhedral structure and are encapsulated by a complex boron network. These transition metal−boron structures fit into holes left by the Pr/Te sublattice resulting in a CsCl-like arrangement. Single crystal X-ray diffraction studies indicate that the compounds are merohedrally twinned. The transition metal boride clusters exhibit two possible orientations; this mandates the use of STEM measurements to determine the true positioning of the atoms. The praseodymium ions and the transition metal structures give rise to long-range magnetic ordering at low temperatures for both analogs. $Pr_{21}Mn_{16}Te_6B_{30}$ exhibits antiferromagnetic ordering at T_N = 15 K, and $Pr_{21}Fe_{16}Te_6B_{30}$ undergoes a likely ferrimagnetic transition at T_C = 23 K. Electronic structure calculations indicate the compounds are metals.

EXPERIMENTAL METHODS

Synthesis. Reactions yielding the new compounds $Pr_{21}Fe_{16}Te_6B_{30}$ and $Pr_{21}Mn_{16}Te_6B_{30}$ were assembled in a drybox under an argon atmosphere. A Pr/Ni flux mixture was made by arc melting chunks of Pr with slugs of Ni (both from Alfa Aesar, 99.9%) in a 3:1 mmol ratio. Inspection of the Pr/Ni phase diagram shows the 3:1 mol ratio forms the congruently melting compound Pr_3Ni (mp 525 °C) on cooling.[25] Arc melting was carried out under an argon atmosphere on a water-cooled copper hearth. Each button of flux was turned over and remelted three times to ensure homogeneous mixing of the metals. The resulting flux ingots were pulverized, yielding pieces up to 1 mm diameter, for use in subsequent reactions.

Elemental powders of Fe, B (both Strem Chemicals, 99.9%), and Te (Cerac, Inc., now Materion, 99.95%) were loaded into an alumina crucible in 1:2:1.5 mmol amounts, sandwiched between 1.5 g of Pr/Ni flux. For reactions substituting manganese for iron, Mn powder from Alfa Aesar (99.6%) was used. The loaded crucible was placed on top of quartz wool resting at the bottom of a silica sleeve. An iron mesh frit was placed on top of the crucible, with more quartz wool placed on top of the frit; the frit and the wool were subsequently used to filter the molten flux from reaction products during centrifugation. The silica ampule was flame-sealed under <100 mTorr vacuum (the contents of the vessel were briefly exposed to air during transfer from the drybox to the vacuum line). The sealed vessel was placed in a box furnace. Reactions were heated to a soak temperature of 1000 °C in 2 h, then held at this temperature for another 10 h, and the vessel was then cooled to 650 °C over 56 h. After the cooling phase of the temperature profile, the reaction vessel was removed from the oven and inverted, and the molten flux was decanted by centrifugation. The reaction vessel was opened to the air and the product matrix inspected with an optical microscope, revealing the title compound which forms as cube-shaped crystals with iridescent reflective surfaces.

Single Crystal X-ray Diffraction (SCXRD). Cube-shaped crystals were cut into fragments of ~1 μm^3, which were mounted on nylon fiber loops with parabar oil and chilled to 200 K under a Cryostream N_2 flow. SCXRD data were collected on a Rigaku Oxford Diffraction XtaLAB Synergy diffractometer with a HyPix-6000HE HPC detector and Mo-target X-ray tube (λ = 0.71073 Å). Unit cell determinations performed on four separate single crystals of $Pr_{21}Fe_{16}Te_6B_{30}$ all yielded similar parameters in the cubic P Bravais lattice. Data were collected as ω scans with a 0.5° step width. Frame integration and data reduction were performed in the CrysAlisPro suite of programs.[26] Analysis of systematic absences by XPREP suggested the centrosymmetric space group $Pm\bar{3}m$ (No. 221). Least squares refinement was performed on $|F^2|$, and a direct methods solution was attempted by means of SHELX.[27] Praseodymium and tellurium positions were indistinguishable by direct methods and had to be assigned based on interatomic distance to the nearest neighbor atoms. Iron (or manganese) and boron were determined from residual electron density peaks in the difference Fourier maps and further refined with reference to interatomic distances. Freely varying the occupancies of all atoms revealed the transition metal and boron sites to be roughly half-occupied, and the transition metal sublattice disorder was analyzed in terms of transition-metal−transition-metal bond distances (see Results and Discussion). Atomic coordinates were standardized with STRUCTURE TIDY.[28] Crystallographic data collection parameters are summarized in Table 1. Further crystallographic data (atomic positions, site occupancy factors, and thermal parameters) for the $Pm\bar{3}m$ and $P\bar{4}3m$ models of $Pr_{21}Fe_{16}Te_6B_{30}$ are found in the Supporting Information.

Table 1. Crystallographic Data Collection Parameters for $Pr_{21}Fe_{16}Te_6B_{30}$ and $Pr_{21}Mn_{16}Te_6B_{30}$

formula	$Pr_{21}Fe_{16}Te_6B_{30}$		$Pr_{21}Mn_{16}Te_6B_{30}$	
formula weight (g mol^{-1})	4942.61		4928.07	
crystal system	cubic		cubic	
space group	$Pm\bar{3}m$	$P\bar{4}3m$	$Pm\bar{3}m$	$P\bar{4}3m$
a (Å)	10.59968(4)		10.61709(5)	
Z	1		1	
volume ($Å^3$)	1190.91(1)		1196.79(2)	
density (g cm^{-3})	6.87145(8)		6.8377(1)	
radiation	Mo Kα (λ = 0.71073 Å)		Mo Kα (λ = 0.71073 Å)	
temperature (K)	200(2)		200(2)	
index ranges	$-21 \le h \le 17$, $-19 \le k \le 12$, $-19 \le l \le 20$		$-15 \le h \le 21$, $-20 \le k \le 18$, $-20 \le l \le 11$	
theta range (deg)	2.718−45.010		1.918 to 44.980	
reflections collected	9606		9781	
unique data/parameters	1041/30	1848/36	1045/30	1866/36
μ (mm^{-1})	29.30		28.52	
R_1/wR_2	0.0196/0.0399	0.0634/0.1916	0.0290/0.0716	0.0489/0.1461
R_1/wR_2 (all data)	0.0202/0.0400	0.0649/0.1935	0.0302/0.0720	0.0504/0.1476
residual peak/hole (e^- $Å^3$)	2.90/−4.97	27.33/−6.96	4.11/−5.14	20.65/−6.19

Electron Microscopy (SEM-EDS and TEM-SAED). Elemental analysis was performed with scanning electron microscopy (SEM), using an FEI Nova 400 NanoSEM with energy dispersive spectroscopy (EDS) capabilities. Single crystals were affixed to carbon tape on aluminum pucks for analysis. The accelerating voltage was set to 30 kV with an accumulation time of 60 s. Data collected on the interior and exterior on crystals of the title compounds gave average molar ratios of Pr/Mn/Te of 52.6(1):32.6(2):14.78(9)% for the manganese-containing variant and Pr/Fe/Te of 48.7(1):38.2(3):13.1(1)% for the iron analog. Trace amounts (<2%) of nickel and silicon were indicated. Nickel was assumed to be either a surface contaminant left over from residual flux or substituting in trace amounts onto iron sites in the structure. The silicon was treated as a contaminant introduced by the silica wool interacting with Te vapors in the headspace of the reaction vessel.

Samples for transmission electron microscopy (TEM) were prepared by crushing several single crystals in ethanol with a mortar and pestle. This ethanol suspension of crushed crystals was then

https://dx.doi.org/10.1021/acs.inorgchem.9b03358
Inorg. Chem. 2020, 59, 2484−2494

dropped with a pipet onto a TEM copper grid coated with a 200 μm mesh carbon/Formvar film. The TEM sample prepared this way preserved the pristine quality of the crystals. High angle annular dark field scanning transmission electron microscopy (HAADF-STEM) was carried out on a probe-aberration-corrected, cold-field-emission JEM JEOL-ARM200cF at 200 kV using a JEOL detector. The STEM resolution is 0.078 nm. Atomic resolution HAADF-STEM images were acquired using a spot size of 0.078 nm, a 30 μm condenser lens aperture, and a camera length of 12 cm, corresponding to an actual inner collection angle of 52 mrad. The image scan speed was 31.5 μs/pixel. The beam convergent angle was 21 mrad.

Magnetic Measurements. Magnetic properties were investigated using a Quantum Design MPMS SQUID magnetometer. Several small crystals of $Pr_{21}Mn_{16}Te_6B_{30}$ were sandwiched between two 4 cm pieces of Kapton tape and then placed inside a plastic sample holder for insertion into the magnetometer. For $Pr_{21}Fe_{16}Te_6B_{30}$, a mosaic of single crystals was mounted on a quartz rod using GE varnish. Field-cooled (FC) and zero-field cooled (ZFC) measurements were collected at a 500 G applied field strength over a temperature range of 1.8 to 300 K. Field-dependence data were collected from 0 to 7 T at both 11 and 50 K for the Mn analogue and at 1.8 K, 10 and 20 K for the Fe analogue.

Electronic Structure Calculations. Density of states (DOS) calculations were carried out for for the $P\bar{4}3m$ structures of both $Pr_{21}M_{16}Te_6B_{30}$ analogs using the tight-binding linear muffin tin orbitals−atomic sphere approximation[29−31] implemented in the Stuttgart TB-LMTO-ASA package.[32] The structural models were based on unit cell parameters and atomic coordinates determined by single crystal X-ray diffraction at 200(2) K. The TB-LMTO-ASA method is known to produce large charge oscillations in d and f orbitals in model systems with lanthanide atoms, leading to difficulty in convergence.[33] Pr atoms were therefore modeled as La. Atomic spheres of the models were space-filling, making the addition of empty spheres unnecessary. An improved tetrahedron method was used to integrate a 16 × 16 × 16 κ-space, giving 249 irreducible κ points in the first Brillouin zone for the model cubic phases. The basis sets for all calculations consisted of 6s/(6p)/5d/4f for La, 5s/5p/(5d)/(4f) for Te, 4s/4p/3d for Fe or Mn, and 2s/2p/(3d) for B, with parenthetical orbitals downfolded.

RESULTS AND DISCUSSION

Synthesis. $Pr_{21}M_{16}Te_6B_{30}$ was obtained from reactions of either iron or manganese with tellurium and boron in a Pr/Ni (3:1) binary flux mixture. Attempts to make these compounds by heating stoichiometric mixtures of the elements were not successful. The Pr/Ni flux reaction procedures reported here allow for the isolation of silver iridescent beveled cubes with volumes between 8 μm^3 and 64 μm^3 (Figure 1). The crystals are stable to air for a week, to water for up to 5 days, and in ethanol up to 10 days, after which time they begin to show signs of deterioration. The major reaction byproduct was PrTe, growing as a polycrystalline powder; this is air-stable up to several weeks. To obtain clean crystals for subsequent measurements, clusters of crystals were placed in 99% ethanol for 5 days to etch away the flux adhering them together; after this, individual crystals of $Pr_{21}Fe_{16}Te_6B_{30}$ could be separated from PrTe powder and residual flux. The crystals were placed under parabar oil and their surfaces scraped of secondary surface phases with a razor blade. Parabar oil and surface particles were washed from the crystal using hexanes. Finally, the crystals were sonicated in ethanol for 1/2 h.

Structure of $Pr_{21}Fe_{16}Te_6B_{30}$. When $Pr_{21}Fe_{16}Te_6B_{30}$ was analyzed by SCXRD, XPREP initially suggested the $Pm\bar{3}m$ space group and possible merohedral twinning by reference to a low $\langle|E^2 - 1|\rangle$ parameter. A partial structure solution was done in $Pm\bar{3}m$ with good R_1 values, no split or nonpositive definite atoms, and low residual electron densities. This partial

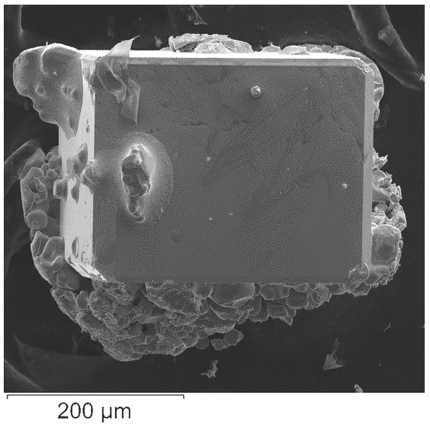

Figure 1. SEM micrograph of a $Pr_{21}Fe_{16}Te_6B_{30}$ sample before cleaning. Specks of residual flux and PrTe can be seen adhering to the surface.

solution featured a well-ordered praseodymium−tellurium sublattice but had half-occupied transition metal sites and too-short distances between symmetry-equivalent transition metal sites and between transition metal and boron sites.

The ordered Pr/Te framework of $Pr_{21}Fe_{16}Te_6B_{30}$ is comprised of one crystallographically unique tellurium site (6f Wyckoff position), surrounded by nine praseodymium atoms in a monocapped square antiprism arrangement (Te(1)@Pr_9). Building blocks consisting of a main group element surrounded by 9−12 rare earth atoms are found in many flux-grown quaternary intermetallics.[34] The 6f position is 3.343−3.380 Å distant from the Pr atoms in the square antiprism and 3.235 Å to the capping Pr atom. These distances are on the order of Pr−Te distances found in Pr_2Te_5 (3.234−3.425 Å)[35] and $PrTe_3$ (3.202−3.367 Å).[36] The capping praseodymium atom, Pr(3), is found at the body center of the unit cell, Wyckoff position 1*a*. This atom caps six Te@Pr_9 units and lies at the intersection of three orthogonal chains of monocapped square antiprisms. Each chain is parallel to a unit cell direction and alternately corner-shares a capping atom and shares the square faces opposite the capping atom. The resulting Pr/Te network defines voids in which the iron boride clusters are located. The overall positioning of groups of six apex-sharing Pr/Te units and the Fe/B clusters occurs in a CsCl arrangement, as highlighted in Figure 2.

Two unique iron sites are found in the structure. Fe(2) (Wyckoff site 8*g*) positions form a cube that is centered on the

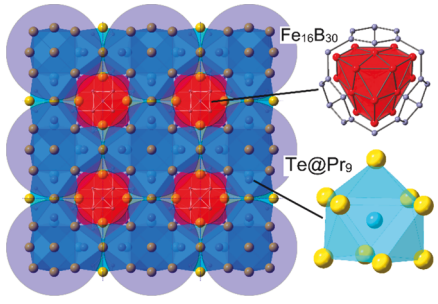

Figure 2. Projection of $Pr_{21}Fe_{16}Te_6B_{30}$ structure down the [100] axis. Circles illustrate CsCl-like structure, with blue circles indicating groups of six Te@Pr_9 clusters and red circles indicating $Fe_{16}B_{30}$ clusters. Local structures are detailed on the right.

https://dx.doi.org/10.1021/acs.inorgchem.9b03358
Inorg. Chem. 2020, 59, 2484−2494

unit cell corners; this cube is encapsulated by a rhombicuboctahedron of Fe(1) positions (Wyckoff site 24*m*). A rhombicuboctahedron may be thought of as a uniformly cantellated cube. Bevelling each vertex and edge of a cube produces triangular and rectangular faces, respectively. Each cube corner becomes a triangular face comprised of three vertices, for a total of 3 × 8 = 24 new vertices in the rhombicuboctahedron. For each Fe(2) cube corner in the crystal structure, there is a capping triangular face of Fe(1) positions on the rhombicuboctahedron. The distances between the corners of this triangle (2.48 Å) are in good agreement with reported Fe−Fe distances, but the distance of each to the cube corner is too short (1.645 Å). Nearest neighbor corners of the Fe(2) cube are again too short (2.135 Å) to each contain Fe atoms. If a Fe(2) cube corner is occupied by an Fe atom, the adjacent Fe(1) triangular face cannot be occupied. This conundrum is solved by the observed half-occupancy of the iron sites.

By selecting first one Fe(2) position and designating it as occupied, it must be the case that nearest neighbor cube corners are unoccupied, as are the vertices of the nearest neighbor rhombicuboctahedron triangle face. A process of elimination then dictates that the cube of Fe(2) positions is in fact two tetrahedra of iron atoms, only one of which is occupied; while the rhombicuboctahedron of Fe(1) positions is instead a truncated tetrahedron of iron atoms, for a total of (8 + 24)/2 = 16 iron atoms per unit cell (see Figure 3). The four atoms of the inner tetrahedron occupy positions centered on, but slightly out of plane of, each hexagonal face of the truncated tetrahedron.

A structure model in space group *P*1 (#1) was built in SHELX with the so-defined 16-atom iron cluster as well as all praseodymium and tellurium atoms. The TwinRotMat subroutine of PLATON[37] was invoked, but no applicable twin laws were found. The XPREP-suggested twin law (0 1 0 1 0 0 0 0 −1) and a racemic twin law were tested in the structure files, but neither law stabilized the R_1 value of the solution nor dephased residual peak densities.

Running ADDSYM[38] on the structure files indicated the Fe_{16} substructure model had $P\bar{4}3m$ local symmetry. Given the positions of the residual peaks, this local structure could have one of two possible orientations, related to each other by inversion symmetry. Several $Pr_{21}M_{16}Te_6B_{30}$ single crystals were analyzed by diffraction, and all exhibited the same structural ambiguities and high residual peak densities in $P\bar{4}3m$. With the XPREP suggestion of merohedral twinning, three possibilities were considered. First, the two orientations could be accounted for by formation of a supercell. This possibility was ruled out by collecting zone photos along each unit cell axis; these did not display any supercell peaks (Figure S1, Supporting Information). Second, there was a statistical (random) distribution of Fe_{16} cluster orientations throughout the crystal. Third, the phase was segregating into twin domains at length scales beneath the size of the smallest observed crystallites (1 μm^3). The latter two possibilities were probed by TEM, *vide infra*.

The structure description which follows is in reference to the $P\bar{4}3m$ model. The Fe_{16} cluster can be formally described as a Friauf polyhedron. $MnZn_2$, an intermetallic compound featuring this structural motif, was first described by James Friauf in 1927.[39] The cluster features 42 triangular faces in three types, designated here as F1, F2, and F3. F3 corresponds to the triangular face of the truncated tetrahedron formed by

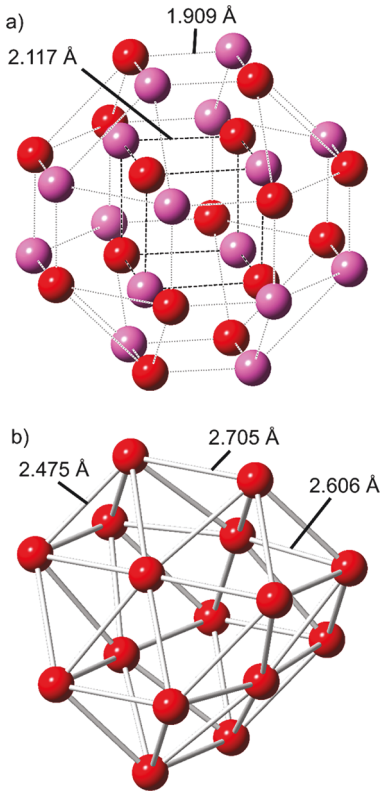

Figure 3. Disorder in the iron sites of $Pr_{21}Fe_{16}Te_6B_{30}$. (a) Schematic of two superimposed Fe_{16} clusters; the averaged overall structure has $Pm\bar{3}m$ symmetry. Red positions give one orientation with $P\bar{4}3m$ symmetry; pink positions give the other orientation. Either pink positions or red positions may be occupied, but not both, for bond lengths to be physically realistic. (b) Individual $P\bar{4}3m$ symmetry Fe_{16} cluster with reasonable bonds indicated.

Fe(1) sites. The Fe(2) atoms are positioned in the center of each hexagonal face of the truncated tetrahedron; their bonds to adjacent Fe(1) atoms form the F2 and F3 triangular planes. See Figure 4a for an illustration of the overall structure and Figure 4c for that of the $Fe_{16}B_{30}$ local structure.

Fe(2) atoms are 2.601 Å from six occupied Fe(1) positions. The three Fe(1) atoms which define F3 are within suitable distance for Fe−Fe bonds (2.458 Å). For instance, the Fe−Fe distances in Pr_2Fe_{17} are within a range of 2.362−2.723 Å[40] and those in $Pr_2Fe_{14}B$ from 2.388 to 2.798 Å.[41] The longer Fe(1)−Fe(1) contacts of 2.708 Å that bridge the F3 faces are also within the suitable ranges already indicated.[40,41] This Fe−Fe bond is edge-capped by boron (B(3), Wyckoff site 6*g*) at a distance of 2.181 Å to adjacent Fe(1) atoms, longer than Fe−B distances in $Pr_2Fe_{14}B$ (2.099−2.134 Å)[41] but shorter than those found in $Pr_4Fe_3B_6$ (2.271 Å).[42] This boron is in turn bonded to its symmetry equivalent to form a boron−boron dimer which bridges adjacent $Fe_{16}B_{30}$ clusters (see Figure 4b). The B(3)−B(3) interatomic distance is 1.779 Å, shorter than boron−boron distances in $Pr_4Fe_3B_6$ (1.836 Å)[42] but longer than the 1.766 Å distances between boron atoms found in $Pr_{1+\varepsilon}Fe_4B_4$.[43] A square plane is formed by Pr(1) atoms perpendicular to and halfway down the B(3)−B(3) bond length, with Pr(1) atoms equidistant (2.762 Å) to each boron atom, between the Pr−B distances found in $Pr_4Fe_3B_6$ (2.747 Å)[42] and $Pr_{33}Fe_{12.9}Al_{0.1}B_{18}C_{34}$ (2.913−3.058 Å).[21]

Faces F1 and F2 are face-capped by B(1) and B(2), respectively, forming a hexagonal ring of boron atoms hovering

https://dx.doi.org/10.1021/acs.inorgchem.9b03358
Inorg. Chem. 2020, 59, 2484−2494

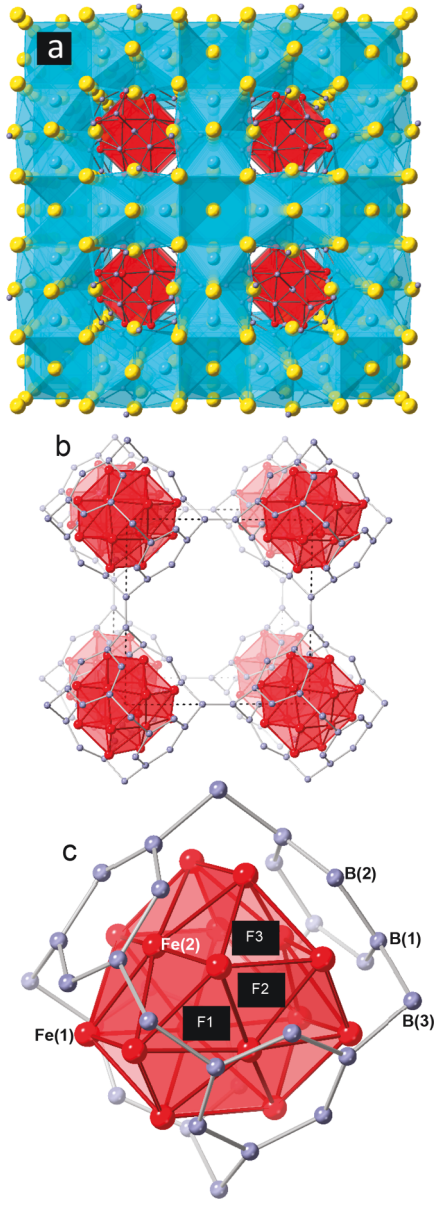

Figure 4. (a) Overall structure of $Pr_{21}Fe_{16}Te_6B_{30}$, with Pr in yellow, Te in blue, Fe in red, and B in lavender. (b) Structure with Pr and Te removed, to show the arrangement of iron clusters and boron network in the unit cell. (c) Illustration of $Fe_{16}B_{30}$ local structure. Faces F1, F2, and F3 of the Fe_{16} Friauf polyhedron arrangement are indicated.

above each hexagonal face of the Fe_{16} cluster. B(2) is 2.099 Å away from each Fe(1) atom and 2.180 Å from Fe(2). The distances between B(3) and these iron atoms are 2.146 and 2.236 Å, respectively. Boron−boron distances around the ring are 1.774 Å. B(3) atoms are connected to B(1) at a distance of 1.898 Å. The hexagonal ring of borons is face-capped by Pr(2), 2.711 Å distant from B(2) and 2.754 Å from B(1). These latter distances are on the shorter end of many reported Pr−B bond lengths but within the ranges found in Pr_2B_5 (2.724−3.022 Å)[44] and $PrMnB_4$ (2.635−2.794 Å).[45] The F3 face is face-capped by the Pr(3) atom; each Fe(1) atom is 2.956 Å distant from the praseodymium. This distance is on the order of Pr−Fe distances found in $Pr_{1+\varepsilon}Fe_4B_4$ (2.902−3.097 Å)[43] and $Pr_6Fe_{13}Ag$ (2.910−3.084 Å).[46]

Important interatomic distances for both the $Pm\bar{3}m$ and $P\bar{4}3m$ models are given in Table 2. Interatomic distance ranges

Table 2. Comparison of Interatomic Distances (Å) between $Pr_{21}Fe_{16}Te_6B_{30}$ $Pm\bar{3}m$ and $P\bar{4}3m$ Structure Models

atom 1−atom 2	$Pm\bar{3}m$	$P\bar{4}3m$
Pr−B	2.707(7)−2.769(3)	2.71(2)−2.79(2)
Pr−Fe	2.959(1)−3.2293(9)	2.956(4)−3.228(3)
Pr−Te	3.2346(5)−3.3801(4)	3.236(1)−3.396(7)
Pr−Pr	3.6981(2)−3.9170(4)	3.698(1)−3.919(2)
Fe−B	0.676(9)−2.283(9)	2.10(2)−2.24(2)
Fe−Fe	1.643(6)−2.461(2)	2.458(5)−2.708(6)
B−B	0.78(2)−1.87(1)	1.77(2)−1.90(3)

for Pr−B, Pr−Fe, Pr−Te, and Pr−Pr are similar between the two models, reflecting the well-ordered nature of the Pr−Te sublattice. The disorder is highlighted by the unrealistically short Fe−B, Fe−Fe, and B−B distances in the $Pm\bar{3}m$ model. The distances between these atoms in the $P\bar{4}3m$ model are, by contrast, physically reasonable.

Transmission Electron Microscopy (TEM). Complementing the long-range averaging of diffraction experiments with a method that allows for probing of local structure can be highly informative. This was exemplified in a report on $AgPb_mSbTe_{2+m}$ materials. By diffraction, these compounds appeared to be a solid solution of PbTe and $AgSbTe_2$, but HRTEM and SAED studies revealed the presence of nanostructuring.[47] Similar studies were carried out on $Pr_{21}Fe_{16}Te_6B_{30}$ to explore the nature of its disorder. A TEM micrograph of a crystal fragment at low magnification is shown in Figure 5a. The lines of contrast are due to fracture ridges formed when the crystal was crushed. The selected area electron diffraction (SAED) pattern along [110] from an area less than 0.5 μm size is shown in Figure 5b. The calculated [110] diffraction patterns from $P\bar{4}3m$ and $Pm\bar{3}m$ structures are shown in Figure 5c and d, respectively. The features that distinguish $P\bar{4}3m$ from $Pm\bar{3}m$ are the relative diffraction intensity difference between {101} and {111}—for $P\bar{4}3m$ symmetry, {101} has lower intensity than {111}; for $Pm\bar{3}m$, {101} has higher intensity. The insets of the calculated diffraction intensity profile clearly demonstrate the intensity difference. In the experimental single crystal diffraction pattern in Figure 5b, {101} intensity is clearly lower than that of {111}, confirming that the selected area of this single crystal has $P\bar{4}3m$ structure. Although the intensity difference is smaller than the calculated perfect structure, it might be due to electron dynamic interaction and Fe_{16} cluster twinning as clarified below.

Higher magnification imaging on the atomic scale was collected along the thin edges of the crystal. HAADF-STEM imaging shows columns of atoms with intensities that are close to proportional to Z^2 of the atoms; there is also a direct relationship with the atom density along that atomic column, where the intensity is higher with more closely spaced atoms in that column. Figure 6a−c show the structure projected along the [100] direction. The most intense columns contain praseodymium and tellurium atoms. Boron atoms with $Z = 5$ are too light to see in this type of image. The four iron atomic columns in the center of the unit cell have an average Fe−Fe spacing of 5.305 Å, whereas the Fe columns near Pr have an average spacing of 10.602 Å along the columns. So the four central Fe columns show much higher intensity and can be clearly seen in Figure 6b. A better viewing direction for the Fe_{16} cluster distribution is along [110]. Figure 6d and f show the projected view along [110] of the $Pm\bar{3}m$ and $P\bar{4}3m$

https://dx.doi.org/10.1021/acs.inorgchem.9b03358
Inorg. Chem. 2020, 59, 2484−2494

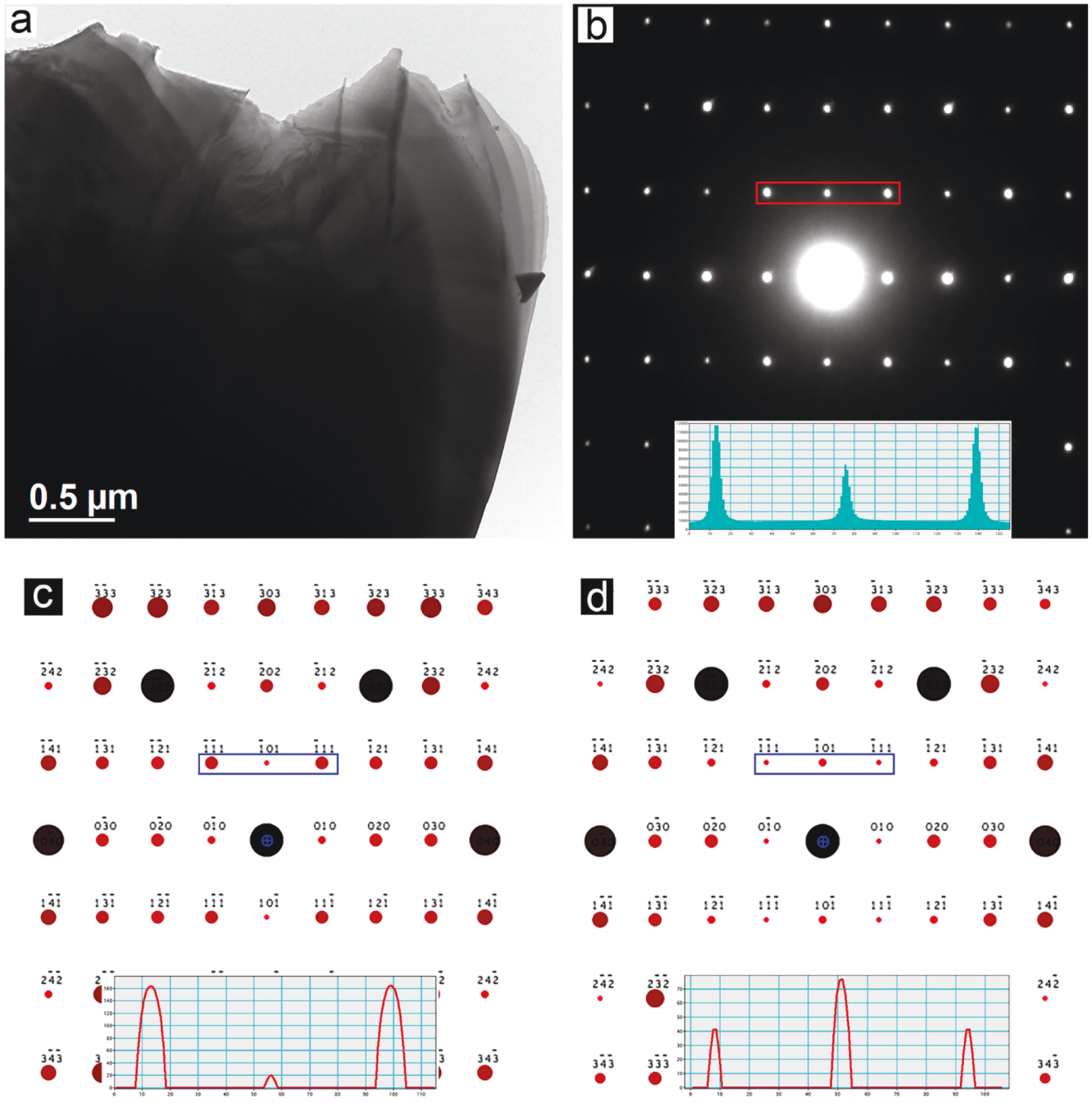

Figure 5. (a) TEM bright field image of a fragment of a $Pr_{21}Fe_{16}Te_6B_{30}$ single crystal. (b) Selected area electron diffraction pattern along the [110] direction. Inset: Diffraction spot intensity profile from three selected diffraction peaks shown in the red box. (c) Calculated [110] diffraction pattern for $P\bar{4}3m$ structure. Inset: Intensity profile of three selected peaks. (d) Calculated [110] diffraction pattern from the $Pm\bar{3}m$ model. Inset: Intensity profile of three selected peaks.

structures, respectively. If the local Fe_{16} orientations are statistically distributed, the column seen down a given axis would exhibit an overlay of the two possible orientations. If, however, a column is well-ordered, we should see only one orientation. Careful inspection of the structure model indicated that differences in local orientation of the transition metal sublattice could be observed down the [110] and its degenerate axes (Figure 6d and f), supporting the $P\bar{4}3m$ model.

In the case that the cluster orientations are statistically distributed ($Pm\bar{3}m$ solution), the average Fe atom spacing along this direction is 14.985 Å. The atoms are further apart if Fe_{16} clusters are in a twin relationship along [110]. Therefore, the Fe_{16} atomic column intensity would be too low to be easily discernible by intensity in the HAADF-STEM image (Figure 6e). However, fast Fourier transform (FFT) of the HAADF-STEM images, which is equivalent to electron diffraction from this 7.5 nm × 7.5 nm area (in contrast to the ca. 500 nm diameter area used for the SAED in Figure 5), can show the difference in {101} diffraction intensity, revealing the Fe_{16} cluster distribution (Figure 7). Figure 7a and b are two HAADF-STEM images from different areas of one single crystal. Their corresponding FFT patterns (Figure 7c and d)

https://dx.doi.org/10.1021/acs.inorgchem.9b03358
Inorg. Chem. 2020, 59, 2484−2494

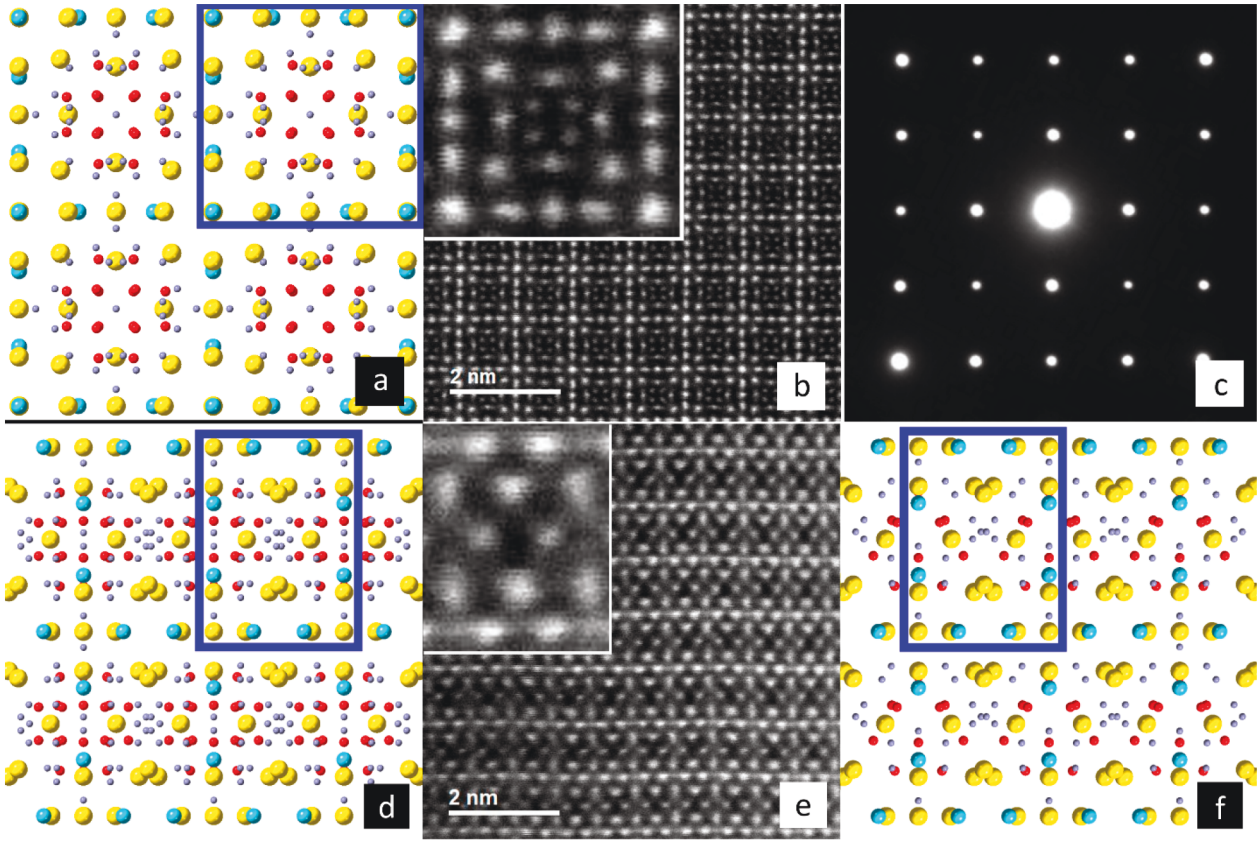

Figure 6. Comparison of $Pm\bar{3}m$ and $P\bar{4}3m$ structure solutions with collected STEM images and SAED diffraction patterns collected on a $Pr_{21}Fe_{16}Te_6B_{30}$ crystal. Schematic views of the structure are pictured, where (a) shows $Pm\bar{3}m$ and $P\bar{4}3m$ viewed down [100] (view along this axis is identical for the two structures), (d) shows the $Pm\bar{3}m$ [110] direction, and (f) gives the $P\bar{4}3m$ [110] direction. STEM images are given in (b) [100] and (e) [110] directions. SAED pattern taken along [100] is shown in (c).

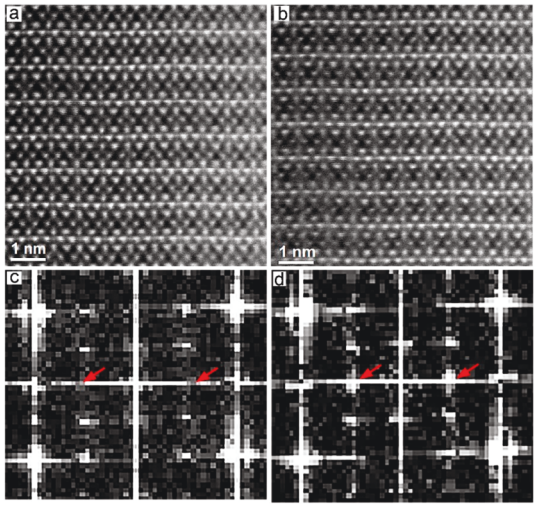

Figure 7. (a and b) Atomic resolution HAADF-STEM images from two different regions of one single crystal of $Pr_{21}Fe_{16}Te_6B_{30}$ viewed down [110]. (c) FFT pattern of region a. (d) FFT pattern of region b. {101} spots are indicated by red arrows.

clearly show {101} spots having different intensity compared to the {111} spots. Figure 7c is typical of $P\bar{4}3m$ structure, and Figure 7d indicates the results of the Fe_{16} twinning in an area of several nanometers size. These TEM and STEM results confirm that the orientations of the Fe_{16} clusters are not randomly distributed but are instead aligned in one direction, having $P\bar{4}3m$ structure. The twinning domain could be as small as nanometer size. The averaging seen in the SCXRD data is therefore due to twinning.

Magnetic Properties. Magnetic susceptibility measurements were performed on a collection of single crystals of $Pr_{21}Mn_{16}Te_6B_{30}$ under an applied field strength of H = 500 G. The temperature dependence of the magnetic susceptibility (Figure 8a) shows paramagnetic behavior at high temperatures and a cusp at 15 K, followed by a steep drop in the susceptibility below the transition temperature, indicating a long-range antiferromagnetic ordering transition. When the ZFC data in the paramagnetic region are fit to the Curie–Weiss law, it yields a magnetic moment of 3.87 μ_B per Pr^{3+} cation. This value is somewhat larger than the calculated moment for a free Pr^{3+} ion of 3.58 μ_B. This may indicate the manganese has a small magnetic moment and contributes to the bulk magnetism of the compound. The Weiss constant calculated from the fit of the Curie–Weiss law is −4.5 K. The negative sign and small magnitude is consistent with the antiferromagnetic transition and the low ordering temperature and suggests that coupling interactions between the Pr^{3+} ions are weak. The slight splitting between FC and ZFC curves indicates a minor degree of magnetic frustration.

Magnetization vs field data were also collected and are shown in Figure 8b. The magnetization in the paramagnetic state (50 K) has the expected linear dependence on field. At 11 K, below the ordering temperature, the phase exhibits a complex magnetic response. At low fields, the effective

https://dx.doi.org/10.1021/acs.inorgchem.9b03358
Inorg. Chem. 2020, 59, 2484−2494

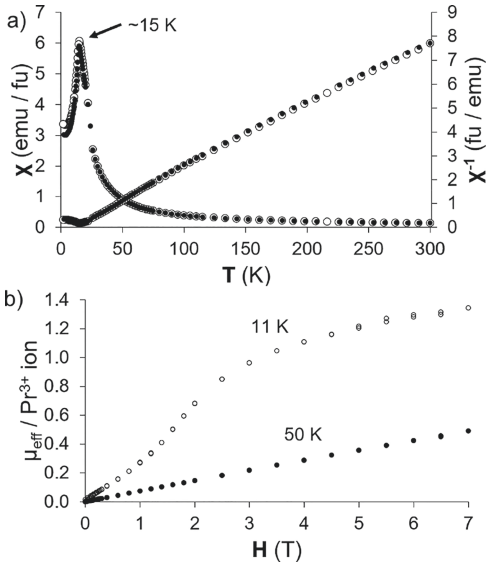

Figure 8. Magnetic susceptibility and magnetization plots for $Pr_{21}Mn_{16}Te_6B_{30}$. (a) Temperature-dependent data under a 500 G applied field. ZFC data shown as solid black dots and FC data as open circles. (b) Magnetization data for $Pr_{21}Mn_{16}Te_6B_{30}$ collected at 11 and 50 K (above and below the transition temperature, respectively).

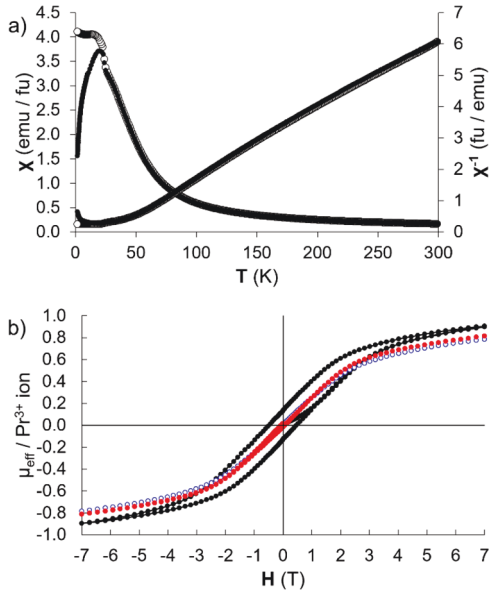

Figure 9. Magnetic susceptibility and magnetization plots for $Pr_{21}Fe_{16}Te_6B_{30}$. (a) Temperature-dependent data under a 500 G applied field. ZFC data shown with solid black symbols; FC data with open symbols. (b) Magnetization data for $Pr_{21}Fe_{16}Te_6B_{30}$ collected at 20, 10, and 1.8 K (open blue circles, red circles, and black circles, respectively).

moment increases gradually with applied field until about 1.5 T, where there is a steeper incline to the response until 3 T is reached. Above this applied field strength, the response begins to level off but does not reach saturation even at 7 T. The complex behavior is likely due to competing antiferromagnetic coupling forces between multiple Pr^{3+} sites leading to a metamagnetic transition to a different ordered state at high fields. No hysteresis is observed in the 11 K field sweep; the magnetization curve from 7 T to lower fields traces back over the curve created during measurements at increasing strength. Hence, only one quadrant is shown.

Similar measurements were carried out on the iron analog, $Pr_{21}Fe_{16}Te_6B_{30}$, under an applied field strength of 500 G; data are shown in Figure 9a. Paramagnetic behavior is observed down to 23 K, at which point a cusp and clear FC-ZFC splitting is seen. Fitting the ZFC data in the paramagnetic region to the Curie–Weiss law indicates a magnetic moment of 4.2 μ_B per Pr^{3+} cation, clearly larger than the moment expected for the Pr^{3+} ion of 3.58 μ_B. This indicates that the iron atoms in the $Fe_{16}B_{30}$ clusters have a magnetic moment. The Weiss constant determined from the Curie–Weiss fit is 16 K. The positive sign supports the presence of ferromagnetic exchange interactions, indicating that the transition at 23 K is either ferro- or ferrimagnetic ordering. The resultant formation of magnetic domains would account for the large FC/ZFC splitting.

Magnetization measurements were carried out at several temperatures to further explore this. The data collected at temperatures below T_C show a gradually increasing hysteresis (none at 20 K, slight at 10 K, and significant at 1.8 K). While the data at 1.8 K do not reach saturation, the compound has a coercive field of 0.45 T and a remnant magnetization of 0.13 μ_B/Pr^{3+}. The lack of saturation and relatively low moment at the highest field measured indicates the ordering is likely ferrimagnetic in nature, with competing coupling forces inducing the multiple magnetic moments (from several Pr and Fe sites) to partially cancel each other. It would be of interest to determine if the magnetic ordering causes strain at the twin boundaries in the crystals from misalignment of easy magnetic axes, although the low Curie temperature and cubic symmetry of the compound make it unlikely that any magnetic field induced reorientation of twin variants would take place.

Electronic Structure Calculations. Density of states calculations were carried out for the model compounds $La_{21}Fe_{16}Te_6B_{30}$ and $La_{21}Mn_{16}Te_6B_{30}$ with $P\bar{4}3m$ symmetry. DOS diagrams for both compounds are shown in Figure 10. The plots feature transition metal bands crossing the Fermi level, overlapping with a moderate contribution from Pr,

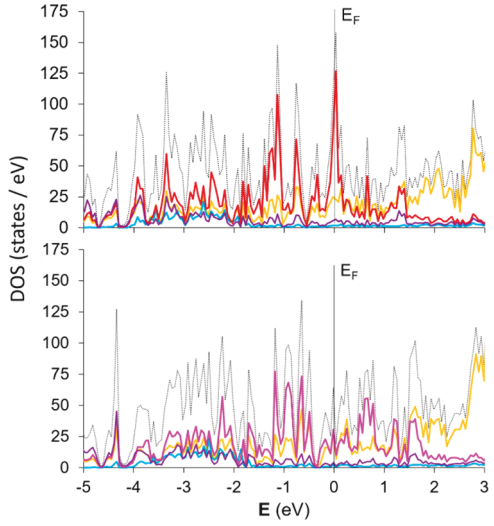

Figure 10. Density of states data for $La_{21}Fe_{16}Te_6B_{30}$ (top) and $La_{21}Mn_{16}Te_6B_{30}$ (bottom). In both plots, partial DOS from B states are represented in purple, Te in blue, iron in red, manganese in fuschia, and La in yellow, with total DOS rendered as a black dashed line. Fermi level is located at 0 eV, indicated by vertical dashed line.

https://dx.doi.org/10.1021/acs.inorgchem.9b03358
Inorg. Chem. 2020, 59, 2484–2494

indicating the compounds are metallic. It is notable that there is a sharp iron d-orbital peak at E_F which may lead to spin polarization and moments developing on the iron atoms. In the manganese analog, the Fermi level does not cut through a sharp Mn peak. This supports the observation of a significant contribution to the magnetic moment from the iron indicated by the magnetic susceptibility data for $Pr_{21}Fe_{16}Te_6B_{30}$, and a much smaller/negligible contribution from the manganese in $Pr_{21}Mn_{16}Te_6B_{30}$. Boron states are diffuse from the Fermi level to −3 eV, beneath which the bands become taller and sharper, suggesting a mixed ionic−covalent character to boron's interaction with the transition metals. The tellurium bands are largely found in the −1.5 to −4.5 eV region with strong overlap with lanthanum states, in agreement with their somewhat anionic nature and coordination by rare earth cations.

CONCLUSION

Rare earth/nickel mixed metal fluxes dissolve boron, leading to the formation of novel intermetallic borides. Reactions of boron, tellurium, and iron or manganese in Pr/Ni flux yielded $Pr_{21}M_{16}Te_6B_{30}$ (M = Mn, Fe) with a new structure type. Other quaternary intermetallic structure types, such as $RE_{21}M_8M_7'C_{12}$ (RE = La−Nd; M = Fe or Mn; M′ = Si, Ge, Sn, Pb, As, Sb, Bi, Te), have exhibited a large amount of flexibility with respect to the types of atoms they can accommodate.[48] In light of this fact, flux reactions targeting $Pr_{21}M_{16}X_6B_{30}$ with smaller chalcogenides (X = Se or S) were carried out but did not produce the same structure. The growth of $RE_{21}M_{16}Te_6B_{30}$ analogs was attempted with La- and Ce-based eutectic fluxes, but neither of these reactions produced the phase of interest. Preliminary work with a Nd/Ni flux, on the other hand, indicates it is possible to produce $Nd_{21}Fe_{16}Sb_6B_{30}$; it is somewhat surprising that an analog with a smaller rare earth metal (Nd) incorporates a larger main group element (Sb). There is an interest to see if the smaller late rare earths (Gd and beyond) can also be fit into this structure; however these RE/Ni eutectics are significantly higher melting than those of the early rare earths, which hinders their use as fluxes.

Complex transition metal clusters composed of numerous edge-sharing transition metal triangles suggest the possibility of magnetically interesting behavior. Reactions of iron and main group elements in rare earth/transition metal eutectics have yielded several new phases featuring iron atoms, clusters, and layers capped by light elements.[32] The magnetic behavior of iron in these RE/Fe/M/M′ compounds correlates with the extent of Fe−Fe bonding. No moment is seen on iron in compounds with little or no Fe−Fe interactions (for instance, $Pr_{61}Fe_{21}Si_{16}C_{32}$).[49] Compounds with Fe_n clusters where $n \geq 4$ do exhibit a magnetic moment on iron, often leading to complex magnetic behavior such as spin glass formation in $La_{21}Fe_8Sn_7C_{12}$,[48] ferromagnetism in $Ce_{33}Fe_{13}B_{18}C_{34}$,[21] and the ferrimagnetism observed in this work for $Pr_{21}Fe_{16}Te_6B_{30}$. There is a clear need to optimize the yield and crystal size of these iron-containing intermetallics. Growth of large crystals (using ^{11}B enriched boron) would be useful for neutron diffraction measurements, which could detect the size and orientation of magnetic moments on specific atoms in the structure. The fact that the merohedral twinning inherent in this structure type occurs in the positioning of the magnetic $Fe_{16}B_{30}$ clusters leads to the possibility of modification of this twinning by annealing in an applied magnetic field.

ASSOCIATED CONTENT

Supporting Information

The Supporting Information is available free of charge at https://pubs.acs.org/doi/10.1021/acs.inorgchem.9b03358.

Tables of atomic coordinates and site occupancies for both structures, and zone photos of diffraction along different axes for $Pr_{21}Fe_{16}Te_6B_{30}$ (PDF)

Accession Codes

CCDC 1965990−1965993 contain the supplementary crystallographic data for this paper. These data can be obtained free of charge via www.ccdc.cam.ac.uk/data_request/cif, or by emailing data_request@ccdc.cam.ac.uk, or by contacting The Cambridge Crystallographic Data Centre, 12 Union Road, Cambridge CB2 1EZ, UK; fax: +44 1223 336033.

AUTHOR INFORMATION

Corresponding Author

Susan E. Latturner − *Department of Chemistry and Biochemistry, Florida State University, Tallahassee, Florida 32306, United States;* orcid.org/0000-0002-6146-5333; Email: latturner@chem.fsu.edu

Authors

Tate O. Engstrand − *Department of Chemistry and Biochemistry, Florida State University, Tallahassee, Florida 32306, United States*

Kaya Wei − *Department of Physics and National High Magnetic Field Laboratory, Florida State University, Tallahassee, Florida 32306, United States*

Ryan Baumbach − *Department of Physics and National High Magnetic Field Laboratory, Florida State University, Tallahassee, Florida 32306, United States*

Yan Xin − *National High Magnetic Field Laboratory, Florida State University, Tallahassee, Florida 32310, United States*

Complete contact information is available at: https://pubs.acs.org/10.1021/acs.inorgchem.9b03358

Notes

The authors declare no competing financial interest.

ACKNOWLEDGMENTS

This research was supported by the Division of Materials Research of the National Science Foundation (Grant Number DMR-14-10214 and DMR-18-08471). This work utilized the scanning electron microscope facilities of the Biological Sciences Imaging Resource (BSIR) in the FSU Biology Department. We thank Dr. Eric Lochner for his assistance with this equipment. TEM work and magnetic susceptibility measurements were performed at the National High Magnetic Field Laboratory, which is supported by National Science Foundation Cooperative Agreement No. DMR-1644779 and the State of Florida.

REFERENCES

(1) Scheifers, J. P.; Zhang, Y.; Fokwa, B. P. T. Boron: Enabling Exciting Metal-Rich Structures and Magnetic Properties. *Acc. Chem. Res.* **2017**, *50* (9), 2317−2325.

(2) Akopov, G.; Yeung, M. T.; Kaner, R. B. Rediscovering the Crystal Chemistry of Borides. *Adv. Mater.* **2017**, *29* (21), 1604506.

(3) Wagner, F. R.; Zheng, Q.; Gumeniuk, R.; Bende, D.; Prots, Y.; Bobnar, M.; Hu, D.-L.; Burkhardt, U.; Grin, Y.; Leithe-Jasper, A. Hierarchical and chemical space partitioning in new intermetallic

borides $MNi_{21}B_{20}$ (M = In, Sn). *Dalton Trans.* **2017**, *46*, 13446−13455.
(4) Mbarki, M.; Touzani, R. St.; Rehorn, C. W. G.; Gladisch, F. C.; Fokwa, B. P. T. New ternary tantalum borides containing boron dumbbells: Experimental and theoretical studies of Ta_2OsB_2 and TaRuB. *J. Solid State Chem.* **2016**, *242*, 28−33.
(5) St. Touzani, R.; Mbarki, M.; Chen, X.; Fokwa, B. P. T. Peierls-Distorted Ru-Chains and Boron Dumbbells in Nb_2RuB_2 and Ta_2RuB_2 from First-Principles Calculations and Experiments. *Eur. J. Inorg. Chem.* **2016**, *2016* (25), 4104−4110.
(6) Mbarki, M.; St. Touzani, R.; Fokwa, B. P. T. Unexpected Synergy between Magnetic Iron Chains and Stacked B_6 Rings in $Nb_6Fe_{1-x}Ir_{6+x}B_8$. *Angew. Chem., Int. Ed.* **2014**, *53* (48), 13174−13177.
(7) Fokwa, B. P. T.; Hermus, M. All-Boron Planar B_6 Ring in the Solid-State Phase $Ti_7Rh_4Ir_2B_8$. *Angew. Chem., Int. Ed.* **2012**, *51* (7), 1702−1705.
(8) Minyaev, R. M.; Hoffmann, R. Transition-Metal Borides with the Ta_3B_4 Crystal Structure: Their Electronic and Bonding Properties. *Chem. Mater.* **1991**, *3* (3), 547−557.
(9) Liang, Y.; Fu, Z.; Yuan, X.; Wang, S.; Zhong, Z.; Zhang, W. An unexpected softening from WB_3 to WB_4. *EPL.* **2012**, *98* (6), 66004.
(10) Wu, L.; Wan, B.; Liu, H.; Gou, H.; Yao, Y.; Li, Z.; Zhang, J.; Gao, F.; Mao, H. Coexistence of Superconductivity and Superhardness in Beryllium Hexaboride Driven by Inherent Multicenter Bonding. *J. Phys. Chem. Lett.* **2016**, *7* (23), 4898−4904.
(11) Korsukova, M. M.; Lundström, T.; Gurin, V. T.; Tergenius, L.-E. An X-ray diffraction study of LaB_6 single crystals, prepared by high-temperature solution growth. *Z. Kristallogr. Cryst. Mater.* **1984**, *168*, 299−306.
(12) Richards, S. M.; Kaspar, J. S. The Crystal Structure of YB_{66}. *Acta Crystallogr., Sect. B: Struct. Crystallogr. Cryst. Chem.* **1969**, *25*, 237−251.
(13) Akopov, G.; Pangilinan, L. E.; Mohammadi, R.; Kaner, R. B. Perspective: Superhard metal borides: A look forward. *APL Mater.* **2018**, *6*, No. 070901.
(14) Markovskii, L. Y. The chemical stability and structure of borides. *Sov. Powder Metall.* **1964**, *1* (4), 256−261.
(15) Hoffmann, R.-D.; Jeitschko, W.; Boonk, L. Structural, Chemical, and Physical Properties of Rare-Earth Metal Rhodium Carbides $LnRhC_2$ (Ln = La, Ce, Pr, Nd, Sm). *Chem. Mater.* **1989**, *1* (6), 580−586.
(16) Kim, D. J.; Thomas, S.; Grant, T.; Botimer, J.; Fisk, Z.; Xia, J. Surface Hall Effect and Nonlocal Transport in SmB_6: Evidence for Surface Conduction. *Sci. Rep.* **2013**, *3*, 3150.
(17) Sussardi, A.; Tanaka, T.; Khan, A. U.; Schlapbach, L.; Mori, T. Enhanced thermoelectric properties of samarium boride. *J. Materiomics.* **2015**, *1* (3), 196−204.
(18) Kitamura, M.; Yoshikawa, H.; Tanaka, T.; Mochizuki, T.; Vlaicu, A. M.; Nisawa, A.; Yagi, N.; Okui, M.; Kimura, M.; Fukushima, S. Non-existence of positive glitches in spectra using the YB_{66} double-crystal monochromator of BL15XU at SPring-8. *J. Synchrotron Radiat.* **2003**, *10*, 310−312.
(19) Herbst, J. F.; Croat, J. J.; Pinkerton, F. E.; Yelon, W. B. Relationships between crystal structure and magnetic properties in $Nd_2Fe_{14}B$. *Phys. Rev. B: Condens. Matter Mater. Phys.* **1984**, *29* (7), 4176−4178.
(20) Kishore, R. A.; Priya, S. Low-grade waste heat recovery using the reverse magnetocaloric effect. *Sustainable Energy Fuels.* **2017**, *1*, 1899−1908.
(21) Tucker, P. C.; Nyffeler, J.; Chen, B.; Ozarowski, A.; Stillwell, R.; Latturner, S. E. A Tale of Two Metals: New Cerium Iron Borocarbide Intermetallics Grown from Rare-Earth/Transition Metal Eutectic Fluxes. *J. Am. Chem. Soc.* **2012**, *134* (29), 12138−12148.
(22) Brgoch, J.; Goerens, C.; Fokwa, B. P. T.; Miller, G. J. Scaffolding, Ladders, Chains, and Rare Ferrimagnetism in Intermetallic Borides: Electronic Structure Calculations and Magnetic Ordering. *J. Am. Chem. Soc.* **2011**, *133* (7), 6832−6840.
(23) Ullakko, K.; Huang, J. K.; Kantner, C.; O'Handley, R. C.; Kokorin, V. V. Large magnetic-field induced strains in Ni_2MnGa single crystals. *Appl. Phys. Lett.* **1996**, *69*, 1966−1968.
(24) Ranzieri, P.; Campanini, M.; Fabbrici, S.; Nasi, L.; Casoli, F.; Cabassi, R.; Buffagni, E.; Grillo, V.; Magen, C.; Celegato, F.; Barrera, G.; Tiberto, P.; Albertini, F. Achieving Giant Magnetically Induced Reorientation of Martensitic Variants in Magnetic Shape-Memory Ni−Mn−Ga Films by Microstructure Engineering. *Adv. Mater.* **2015**, *27*, 4760−4766.
(25) *Binary Alloy Phase Diagrams*, 2nd edition, version 1.0; ASM International: Materials Park, OH, 1996.
(26) *CrysAlisPRO*, version 40; Oxford Diffraction/Agilent Technologies UK Ltd.: Yarnton, England.
(27) Sheldrick, G. M. A short history of SHELX. *Acta Crystallogr., Sect. A: Found. Crystallogr.* **2008**, *A64*, 112−122.
(28) Gelato, L. M.; Parthé, E. STRUCTURE TIDY − a computer program to standardize crystal structure data. *J. Appl. Crystallogr.* **1987**, *20*, 139−143.
(29) Andersen, O. K. Linear Methods in Band Theory. *Phys. Rev. B: Condens. Matter Mater. Phys.* **1975**, *12*, 3060−3083.
(30) Skriver, H. *The LMTO Method: Muffin-Tin Orbitals and Electronic Structure*; Berlin, S.-V., Ed.; Springer-Verlag: Berlin, 1984.
(31) Andersen, O. K.; Jepsen, O. Explicit, First-Principles Tight-Binding Theory. *Phys. Rev. Lett.* **1984**, *53*, 2571−2574.
(32) Krier, G.; Jepsen, O.; Burkhardt, A.; Andersen, O. K. *The TB-LMTO-ASA program*, version 4.7; Stuttgart, Germany; 2000.
(33) Dederichs, P. H.; Zeller, R. Self-consistency iterations in electronic-structure calculations. *Phys. Rev. B: Condens. Matter Mater. Phys.* **1983**, *28*, 5462−5472.
(34) Latturner, S. E. Clusters, Assemble: Growth of Intermetallic Compounds from Metal Flux Reactions. *Acc. Chem. Res.* **2018**, *51*, 40−48.
(35) Pardo, M. P.; Flahaut, J. Les tellurures superieurs des elements des terres rares, de formules L_2Te_5 et LTe_3. *Bull. Soc. Chim. Fr.* **1967**, 3658−3664.
(36) Malliakas, C.; Billinge, S. J. L.; Kim, H.-J.; Kanatzidis, M. G. Square nets of tellurium: rare-earth dependent variation in the charge-density wave of $RETe_3$ (RE = rare-earth element). *J. Am. Chem. Soc.* **2005**, *127* (18), 6510−6511.
(37) Spek, A. L. Structure validation in chemical crystallography. *Acta Crystallogr., Sect. D: Biol. Crystallogr.* **2009**, *D65*, 148−155.
(38) Le Page, Y. Computer derivation of the symmetry elements implied in a structure description. *J. Appl. Crystallogr.* **1987**, *20*, 264−269.
(39) Friauf, J. B. The crystal structures of two intermetallic compounds. *J. Am. Chem. Soc.* **1927**, *49* (12), 3107−3114.
(40) Calestani, G.; Magnani, N.; Paoluzi, A.; Pareti, L.; Rizzoli, C. Structural features of the intermetallic compounds Pr_2M_{17} (M = Fe, Co) and implications on magnetic properties. *Phys. Rev. B: Condens. Matter Mater. Phys.* **2003**, *68*, No. 054424.
(41) Herbst, J. F.; Yelon, W. B. Crystal and magnetic structure of $Pr_2Fe_{14}B$ and $Dy_2Fe_{14}B$. *J. Appl. Phys.* **1985**, *57*, 2343−2345.
(42) Dub, O. M.; Chaban, N. F.; Kuz'ma, Yu. B. New borides of $Pr_{5-x}Co_{2+x}B_6$-type structure containing iron and cobalt. *J. Less-Common Met.* **1986**, *117*, 297−303.
(43) Givord, D.; Tenaud, P.; Moreau, J. M. Modulation of the iron tetrahedra driven by interactions with R atoms in $R_{1+x}Fe_4B_4$ compounds. *J. Less-Common Met.* **1986**, *115*, L7−L10.
(44) Kuz'ma, Y. B.; Babizhetskii, V. S.; Guerin, R.; Mikhalenko, S. I. Crystal structure of Pr_2B_5 boride. *Kristallografiya.* **2003**, *48* (4), 619−623.
(45) Mikhalenko, S. I.; Kuz'ma, Yu. B.; Chuchman, T. D. Reaction in the ternary systems Pr-Mn-B and Nd-Mn-B. *Inorg. Mater. USSR.* **1990**, *26*, 1968−1972.
(46) Schobinger-Papamantellos, P.; Buschow, K. H. J.; de Groot, C. H.; de Boer, F. R.; Ritter, C.; Fauth, F.; Boettger, G. On the magnetic ordering of $R_6Fe_{13}X$ compounds. *J. Alloys Compd.* **1998**, *280*, 44−55.
(47) Quarez, E.; Hsu, K.-F.; Pcionek, R.; Frangis, N.; Polychroniadis, E. K.; Kanatzidis, M. G. Nanostructuring, compositional fluctuations,

https://dx.doi.org/10.1021/acs.inorgchem.9b03358
Inorg. Chem. 2020, 59, 2484−2494

and atomic ordering in the thermoelectric materials $AgPb_mSbTe_{2+m}$. The myth of solid solutions. *J. Am. Chem. Soc.* **2005**, *127*, 9177−9190.
(48) Benbow, E. M.; Dalal, N. S.; Latturner, S. E. Spin Glass Behavior of Isolated, Geometrically Frustrated Tetrahedra of Iron Atoms in the Intermetallic $La_{21}Fe_8Sn_7C_{12}$. *J. Am. Chem. Soc.* **2009**, *131* (9), 3349−3354.
(49) Engstrand, T. O.; Latturner, S. E. $Pr_{62}Fe_{21}M_6C_{32}$ Versus $Pr_{21}Fe_8M'_7C_{12}$ (M = Si, P; M' = Si, Ge, Sn): Competing Intermetallic Carbides Grown from a Pr/Ni Flux. *Inorg. Chem.* **2019**, *58* (1), 540−548.

https://dx.doi.org/10.1021/acs.inorgchem.9b03358
Inorg. Chem. 2020, 59, 2484−2494